

# Refraction effect in an in-plane-switching blue phase liquid crystal cell

Daming Xu, Yuan Chen, Yifan Liu, and Shin-Tson Wu\*

College of Optics and Photonics, University of Central Florida, Orlando, Florida 32816, USA

\*swu@creol.ucf.edu

**Abstract:** We develop a refraction model to analyze the electro-optic effects of an in-plane-switching blue phase liquid crystal (IPS-BPLC) cell. Good agreement with experiment is obtained. Based on this model, we optimize the parameters affecting the electro-optics of IPS-BPLC, such as electrode dimension, saturated induced birefringence, saturation electric field, and cell gap. An IPS-BPLC with low operation voltage ( $<10V_{\text{rms}}$ ) and high transmittance ( $\sim 80\%$ ) with single gamma curve can be achieved by optimizing the BPLC material and device structure.

©2013 Optical Society of America

OCIS codes: (160.3710) Liquid crystals; (230.3720) Liquid crystal devices.

---

## References and links

1. H. Kikuchi, M. Yokota, Y. Hisakado, H. Yang, and T. Kajiyama, "Polymer-stabilized liquid crystal blue phases," *Nat. Mater.* **1**(1), 64–68 (2002).
2. S. W. Choi, S. Yamamoto, Y. Haseba, H. Higuchi, and H. Kikuchi, "Optically isotropic-nanostructured liquid crystal composite with high Kerr constant," *Appl. Phys. Lett.* **92**(4), 043119 (2008).
3. Y. Hisakado, H. Kikuchi, T. Nagamura, and T. Kajiyama, "Large electro-optic Kerr effect in polymer-stabilized liquid-crystalline blue phases," *Adv. Mater.* **17**(1), 96–98 (2005).
4. J. Yan, L. Rao, M. Jiao, Y. Li, H. C. Cheng, and S. T. Wu, "Polymer-stabilized optically isotropic liquid crystals for next-generation display and photonics applications," *J. Mater. Chem.* **21**(22), 7870–7877 (2011).
5. L. Rao, Z. Ge, S. Gauza, K. M. Chen, and S. T. Wu, "Emerging liquid crystal displays based on the Kerr effect," *Mol. Cryst. Liq. Cryst. (Phila. Pa.)* **527**(1), 186–198 (2010).
6. L. Rao, J. Yan, and S. T. Wu, "Prospects of emerging polymer-stabilized blue-phase liquid-crystal displays," *J. Soc. Inf. Disp.* **18**(11), 954–959 (2010).
7. Y. H. Lin, H. S. Chen, H. C. Lin, Y. S. Tsou, H. K. Hsu, and W. Y. Li, "Polarizer-free and fast response microlens arrays using polymer-stabilized blue phase liquid crystals," *Appl. Phys. Lett.* **96**(11), 113505 (2010).
8. J. Yan, Y. Li, and S. T. Wu, "High-efficiency and fast-response tunable phase grating using a blue phase liquid crystal," *Opt. Lett.* **36**(8), 1404–1406 (2011).
9. S. T. Wu and D. K. Yang, *Fundamentals of Liquid Crystal Devices* (John Wiley & Sons, 2006).
10. D. Xu, L. Rao, C. D. Tu, and S. T. Wu, "Nematic liquid crystal display with submillisecond grayscale response time," *J. Disp. Technol.* **9**(2), 67–70 (2013).
11. Y. Chen, F. Peng, and S. T. Wu, "Submillisecond-response vertical-aligned liquid crystal for color sequential projection displays," *J. Disp. Technol.* **9**(2), 78–81 (2013).
12. Y. Chen, J. Yan, J. Sun, S. T. Wu, X. Liang, S. H. Liu, P. J. Hsieh, K. L. Cheng, and J. W. Shiu, "A microsecond-response polymer-stabilized blue phase liquid crystal," *Appl. Phys. Lett.* **99**(20), 201105 (2011).
13. H. Haseba and S. Kobayashi, "A full-color sequential LCD using modulated backlight," *SID Int. Symp. Digest Tech. Papers* **16**, 81–83 (1985).
14. J. H. Lee, X. Zhu, and S. T. Wu, "Novel color-sequential transfective liquid crystal displays," *J. Disp. Technol.* **3**(1), 2–8 (2007).
15. S. Gauza, X. Zhu, W. Piecek, R. Dabrowski, and S. T. Wu, "Fast switching liquid crystals for color-sequential LCDs," *J. Disp. Technol.* **3**(3), 250–252 (2007).
16. Y. Liu, Y. F. Lan, H. Zhang, R. Zhu, D. Xu, C. Y. Tsai, J. K. Lu, N. Sugiura, Y. C. Lin, and S. T. Wu, "Optical rotatory power of polymer-stabilized blue phase liquid crystals," *Appl. Phys. Lett.* **102**(13), 131102 (2013).
17. Z. Ge, S. Gauza, M. Jiao, H. Xianyu, and S. T. Wu, "Electro-optics of polymer-stabilized blue phase liquid crystal displays," *Appl. Phys. Lett.* **94**(10), 101104 (2009).
18. Z. Ge, L. Rao, S. Gauza, and S. T. Wu, "Modeling of blue phase liquid crystal displays," *J. Disp. Technol.* **5**(7), 250–256 (2009).
19. H. C. Cheng, J. Yan, T. Ishinabe, and S. T. Wu, "Vertical field switching for blue-phase liquid crystal devices," *Appl. Phys. Lett.* **98**(26), 261102 (2011).

20. H. C. Cheng, J. Yan, T. Ishinabe, N. Sugiura, C. Y. Liu, T. H. Huang, C. Y. Tsai, C. H. Lin, and S. T. Wu, "Blue-phase liquid crystal displays with vertical field switching," *J. Disp. Technol.* **8**(2), 98–103 (2012).
21. L. Rao, Z. Ge, S. T. Wu, and S. H. Lee, "Low voltage blue-phase liquid crystal displays," *Appl. Phys. Lett.* **95**(23), 231101 (2009).
22. K. M. Chen, S. Gauza, H. Xianyu, and S. T. Wu, "Hysteresis effects in blue-phase liquid crystals," *J. Disp. Technol.* **6**(8), 318–322 (2010).
23. L. Rao, J. Yan, S. T. Wu, S. Yamamoto, and Y. Haseba, "A large Kerr constant polymer-stabilized blue phase liquid crystal," *Appl. Phys. Lett.* **98**(8), 081109 (2011).
24. Y. Chen, D. Xu, S. T. Wu, S. Yamamoto, and Y. Haseba, "A low voltage and submillisecond-response polymer-stabilized blue phase liquid crystal," *Appl. Phys. Lett.* **102**(14), 141116 (2013).
25. M. Wittek, N. Tanaka, D. Wilkes, M. Bremer, D. Pauluth, J. Canisius, A. Yeh, R. Yan, K. Skjonnemand, and M. Klasen-Memmer, "New materials for polymer-stabilized blue phase," *SID Int. Symp. Digest Tech. Papers* **43**, 25–28 (2012).
26. Y. Haseba, S. Yamamoto, K. Sago, A. Takata, and H. Tobata, "Low-voltage polymer-stabilized blue-phase liquid crystals," *SID Int. Symp. Digest Tech. Papers* **44**, 254–257 (2013).
27. M. Kim, M. S. Kim, B. G. Kang, M. K. Kim, S. Yoon, S. H. Lee, Z. Ge, L. Rao, S. Gauza, and S. T. Wu, "Wall-shaped electrodes for reducing the operation voltage of polymer-stabilized blue phase liquid crystal displays," *J. Phys. D Appl. Phys.* **42**(23), 235502 (2009).
28. L. Rao, H. C. Cheng, and S. T. Wu, "Low voltage blue-phase LCDs with double-penetrating fringe fields," *J. Disp. Technol.* **6**(8), 287–289 (2010).
29. M. Z. Jiao, Y. Li, and S. T. Wu, "Low voltage and high transmittance blue-phase liquid crystal displays with corrugated electrodes," *Appl. Phys. Lett.* **96**(1), 011102 (2010).
30. K. M. Chen, J. Yan, S. T. Wu, Y. P. Chang, C. C. Tsai, and J. W. Shiu, "Electrode dimension effects on blue-phase liquid crystal displays," *J. Disp. Technol.* **7**(7), 362–364 (2011).
31. J. Yan, H. C. Cheng, S. Gauza, Y. Li, M. Jiao, L. Rao, and S. T. Wu, "Extended Kerr effect of polymer-stabilized blue-phase liquid crystals," *Appl. Phys. Lett.* **96**(7), 071105 (2010).
32. S. Yoon, G. H. Yang, P. Nayek, H. Jeong, S. H. Lee, S. H. Hong, H. J. Lee, and S. T. Shin, "Study on the light leakage mechanism of a blue phase liquid crystal cell with oblique interfaces," *J. Phys. D Appl. Phys.* **45**(10), 105304 (2012).
33. C. Y. Tsai, T. J. Tseng, L. Y. Wang, F. C. Yu, Y. F. Lan, P. J. Huang, S. Y. Lin, K. M. Chen, B. S. Tseng, C. W. Kuo, C. H. Lin, J. K. Lu, and N. Sugiura, "Polymer-stabilized blue phase liquid crystal displays applying novel groove cell structure," *SID Int. Symp. Digest Tech. Papers* **44**, 182–183 (2013).
34. P. R. Gerber, "Electro-optical effects of a small-pitch blue-phase system," *Mol. Cryst. Liq. Cryst. (Phila. Pa.)* **116**(3-4), 197–206 (1985).
35. M. Z. Jiao, J. Yan, and S. T. Wu, "Dispersion relation on the Kerr constant of a polymer-stabilized optically isotropic liquid crystal," *Phys. Rev. E Stat. Nonlin. Soft Matter Phys.* **83**(4), 041706 (2011).
36. Y. Li, M. Z. Jiao, and S. T. Wu, "Transflective display using a polymer-stabilized blue-phase liquid crystal," *Opt. Express* **18**(16), 16486–16491 (2010).

## 1. Introduction

Polymer-stabilized blue phase liquid crystal (PS-BPLC) [1–4] is emerging as a promising candidate for next-generation display [5, 6] and photonic devices [7, 8]. Different from mainstream nematic liquid crystals [9–11], PS-BPLC is a self-assembly nanostructure electro-optic medium which exhibits three attractive features: (1) self-assembly process to form three-dimensional lattices without the need of surface alignment layer (e.g., polyimide), (2) microsecond response time [12] resulted from nanoscale (~100 nm) double-twisted cylinder diameter and short coherence length, and (3) optically isotropic dark state. Since no surfactant is needed to generate uniform molecular alignment for PS-BPLC, the device fabrication process can be much simplified. And fast response time is particularly desirable because it not only reduces motion blurs but also enables color-sequential display using RGB LED backlight with negligible color breakup [13–15]. With an isotropic voltage-off state, PS-BPLC is able to achieve high contrast ratio and wide view [16].

In terms of device configuration, both in-plane-switching (IPS) [17, 18] and vertical field switching [19, 20] have been developed. Between these two, IPS is commonly employed because of its simpler backlight system. In an IPS cell, electric field is mainly in lateral direction and the Kerr-effect-induced birefringence is along the electric field direction if the BPLC with a positive dielectric anisotropy ( $\Delta\epsilon > 0$ ) is employed. However, IPS-BPLC mode has three drawbacks: high operation voltage, low transmittance and relatively large hysteresis. High operation voltage originates from that the electric fields are confined near the IPS

electrodes and cannot penetrate deeply into the BPLC bulk [21]. Low transmittance results from the “dead zones” on the top of the electrodes since only the horizontal electric field contributes to the transmittance of the IPS-BPLC cell. Moreover, the electric fields are not uniform in an IPS-BPLC cell, especially in the vicinity of electrode edges, the strong electric fields could cause lattice deformation which in turn leads to hysteresis [22].

To reduce operation voltage and hysteresis, both large Kerr constant BPLC materials [23–26], and modified IPS structures, such as protrusion electrodes [21], wall-shaped electrodes [27], etched electrodes [28], and corrugated electrodes [29] have been proposed. With these combined effects, the on-state voltage can be reduced to <10V. However, the transmittance is still limited to 65–70%. Therefore, to develop a high-transmittance IPS-BPLC with a low operation voltage is urgently needed.

To enhance transmittance, Chen, *et al.* [30] observed an interesting phenomenon during the study of electrode dimension effects on IPS-BPLC. It was reported that by reducing the width ( $w$ ) and gap ( $l$ ) of the IPS electrodes, the operation voltage is reduced while the transmittance keeping above 80%. Such a high transmittance is not expected from the model developed by Ge, *et al.* [17, 18], which predicts the peak transmittance is independent of electrode dimension as long as the same  $l/w$  ratio is used. Meanwhile, IPS-2/4 ( $w = 2\mu\text{m}$  and  $l = 4\mu\text{m}$ ), IPS-5/10 and IPS-5/5 are able to achieve over 80% transmittance in experiment, which is much higher than that predicted by Ge’s model, in which the peak transmittance for  $l/w = 1$  and 2 should be  $\sim 50\%$  and  $\sim 64\%$ , respectively. More recently, Chen, *et al.* [24] reported a low voltage IPS-BPLC with peak transmittance  $\sim 60\%$  for IPS-5/5 cell. Therefore, Ge’s model predicts a lower transmittance than the experimental data.

In this paper, we propose a refraction model to explain the dimension effect of IPS-BPLC and obtain good agreement with experimental data. From this model, the electro-optics of IPS-BPLC on electrode dimension, saturated induced birefringence, saturation electric field, and cell gap is analyzed. Promising approaches for achieving high transmittance and low operation voltage are presented. Finally, a new method for achieving single-gamma IPS-BPLC is also proposed.

## 2. Refraction model

### 2.1 Numerical modeling

In Ge’s model, the incident light is assumed to travel in straight lines in an IPS cell. On the top of IPS electrodes, the electric fields are mainly in the vertical direction. Thus, the transmittance in these regions is very low, known as “dead zones”. Let us take IPS-5/5 cell as an example. According to this model, in a voltage-on state it should have bright and dark lines with nearly the same width. However, it was reported in [30] that the effective aperture ratio for the IPS-5/5 sample is  $\sim 75\%$  rather than  $\sim 50\%$ . This oversized bright region indicates that the LCs near the edges of ITO electrodes also contribute to the overall transmittance. To explain this increased aperture ratio, we need a new model.

According to the extended Kerr model [31], the induced birefringence ( $\Delta n$ ) is dependent on the electric field in an IPS-BPLC cell. Consequently, in a voltage-on state the ordinary index ( $n_o$ ) and extraordinary index ( $n_e$ ) should be different at different positions of the cell. Therefore, the BPLC in an IPS cell cannot be regarded as a uniform medium and the incident light would no longer propagate in a straight path. In our refraction model, we take the nonuniform BPLC profile into account so that the incident light is bent by the refraction effect. In particular, on top of the electrodes the incident light would be refracted toward the center of the electrodes, as depicted in Fig. 1. These refracted rays would have a larger angle with respect to the optic axis of BPLC. Meanwhile, their optical path in the cell would become longer due to the bent propagation direction. These two factors contribute to the increased phase retardation on the top of electrodes, resulting in a higher transmittance.

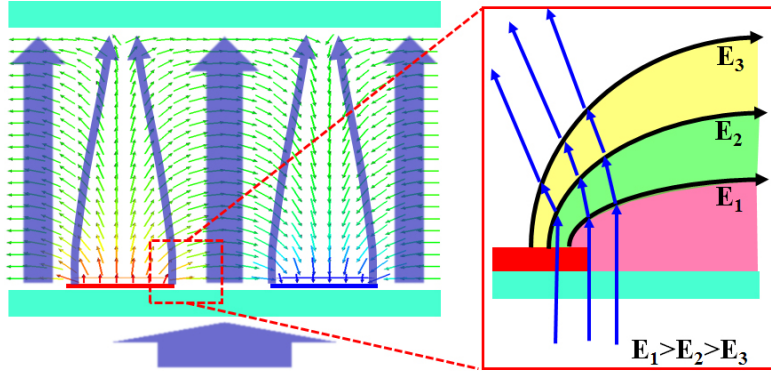


Fig. 1. Principle of refraction effect in IPS-BPLC.

For intensity modulation, an IPS-BPLC cell is placed between two crossed linear polarizers. The electric fields generated from interdigitated pixel electrodes are used to induce phase retardation for the incident light. In the voltage-off state ( $V = 0$ ), BPLC is assumed to be optically isotropic (with refractive index  $n_i$ ), leading to a very good dark state [16]. When an electric field  $\mathbf{E}$  is applied, the induced birefringence is along the electric field direction. Macroscopically speaking, such an isotropic-to-anisotropic transition can be described by the Kerr effect and the induced birefringence characterized by the extended Kerr model [31]:

$$\Delta n = \Delta n_s \left( 1 - \exp \left[ - \left( \frac{E}{E_s} \right)^2 \right] \right), \quad (1)$$

where  $\Delta n_s$  stands for saturated induced birefringence and  $E_s$  the saturation electric field.

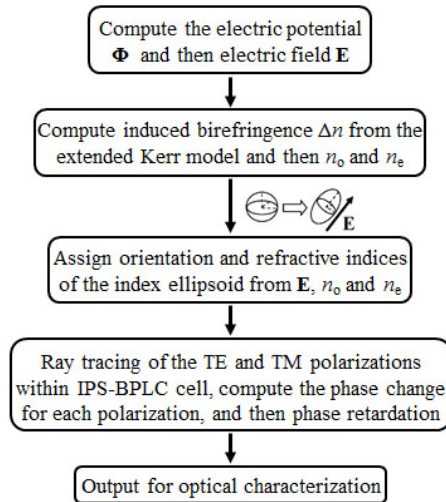


Fig. 2. Flowchart of the IPS-BPLC device modeling based on refraction effect.

Based on the descriptions above, we propose the following flowchart to model the refraction effect, as Fig. 2 depicts. First, we compute the potential distribution by solving the Poisson equation and then the distribution of electric field in the media. This step can be done with commercial software such as DIMOS.2D or TechWiz LCD. In our simulations, we used the electric potential data exported from DIMOS.2D program. To simulate the refraction

effect accurately, we divided the cell into multiple layers with each layer thickness of  $0.1 \mu\text{m}$ . The mesh size on the horizontal direction is  $0.05 \mu\text{m}$ . Next, with the electric field we further calculate the induced birefringence distribution from Eq. (1) and we assume the following equations hold for  $n_e$  and  $n_o$  [31]:

$$n_o = n_i - \frac{1}{3} \Delta n; \quad n_e = n_i + \frac{2}{3} \Delta n. \quad (2)$$

After obtaining  $\mathbf{E}$ ,  $n_e$  and  $n_o$ , we assign the local optic axis direction of each unit along the  $\mathbf{E}$  vector there. Then we trace the paths of the TE and TM polarizations with ray tracing method and compute their phase change and phase retardation. We add this step to Ge's model in order to take refraction effect into account, and the detailed description of this step will be explained in next section. After the phase retardation is calculated, we are able to compute the related electro-optic properties, such as voltage-dependent transmittance (VT) curve.

## 2.2 Modeling physics

When a light passes through the boundary of two uniform isotropic media, the refraction effect is governed by the Snell's law. However, in a voltage-on state the incident light propagates in an anisotropic BPLC medium so that the e-ray (TM) and o-ray (TE) should be considered separately. Since the polarizer is oriented at  $45^\circ$  with respect to the IPS electrodes, the incident linearly polarized light can be decomposed into 50% TE and 50% TM waves. Let's take two arbitrary neighboring layers, the  $m^{\text{th}}$  and  $(m+1)^{\text{th}}$  layers, as an example, among which the  $m^{\text{th}}$  layer is closer to the bottom substrate, as shown in Fig. 3.

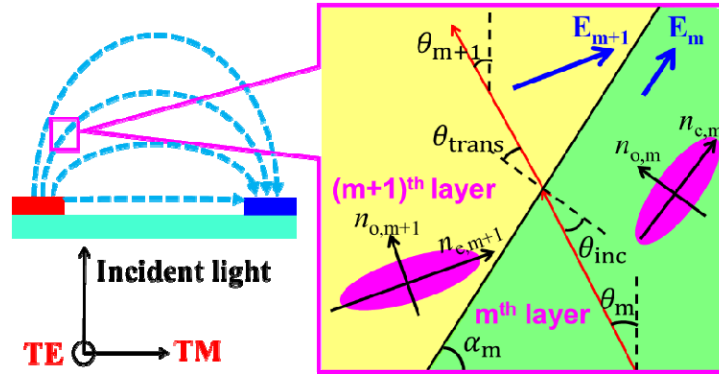


Fig. 3. Refraction at the boundary between the  $m^{\text{th}}$  and  $(m+1)^{\text{th}}$  layers in an IPS-BPLC cell.

For TE polarization, it experiences an ordinary refractive index  $n_o$ . At the interface between these two layers, the incident angle is:

$$\theta_{inc} = \theta_m + \alpha_m, \quad (3)$$

where  $\theta_m$  is the angle between incident light and vertical direction, and  $\alpha_m$  is the inclination angle between the electric field ( $\mathbf{E}_m$ ) and the horizontal axis.

Let us assume  $n_{o,m}$  and  $n_{o,m+1}$  represent the ordinary refractive indices of the  $m^{\text{th}}$  and  $(m+1)^{\text{th}}$  layers, respectively. Because TE polarization is ordinary wave, its refraction effect can still be described by Snell's law:

$$\theta_{trans} = \frac{n_{o,m}}{n_{o,m+1}} \sin(\theta_{inc}). \quad (4)$$

And because the  $m^{\text{th}}$  layer is closer to the electrodes, the electric field in this layer is stronger. According to Eqs. (1) and (2), stronger electric field would result in a larger induced  $\Delta n$  and smaller  $n_o$ . Therefore, the transmitted angle  $\theta_{\text{trans}}$  in the  $(m + 1)^{\text{th}}$  layer is smaller than the incident angle  $\theta_{\text{inc}}$  in the  $m^{\text{th}}$  layer. In the electrode gap, the electric field is nearly horizontal so that  $\theta_{\text{inc}}$  is very small and the refraction effect is negligible, as Eq. (4) indicates. However, on top of the electrodes, the electric fields are tilted along vertical direction. Therefore,  $\theta_{\text{inc}}$  is larger and the light is bent toward the center of electrodes.

The phase change of TE polarization in the  $m^{\text{th}}$  layer can be written as:

$$\varphi_{TE,m} = \frac{2\pi}{\lambda} n_{o,m} t_{TE,m}, \quad (5)$$

where  $t_{TE,m}$  is the optical path of TE polarization in the  $m^{\text{th}}$  layer. The direction of TE polarization in the  $(m + 1)^{\text{th}}$  layer with respect to the vertical direction is

$$\theta_{m+1} = \theta_{\text{trans}} - \alpha_m. \quad (6)$$

We then plug Eq. (6) into Eq. (3) and calculate Eqs. (3)-(6) again for computing the refraction effect of TE polarization in next two layers until the rays arrive at the top substrate.

For TM polarization, the situation is more complicated. The incident angle at the interface between these two layers can still be calculated by Eq. (3). Because the electric field of TM polarization is in the plane of incidence, it's an e-ray propagating in an anisotropic media. Hence, we cannot use Snell's law to determine its transmitted angle. The wave vector  $\mathbf{k}_m$  in the  $m^{\text{th}}$  layer should be determined by following equations:

$$\begin{cases} \frac{k_{\perp C_m,m}^2}{n_{e,m}^2} + \frac{k_{\parallel C_m,m}^2}{n_{o,m}^2} = k_0^2 \\ \frac{k_{\parallel C_m,m}}{k_{\perp C_m,m}} = \tan(\theta_{\text{inc}}) \end{cases}, \quad (7)$$

where  $k_{\perp C_m,m}$  and  $k_{\parallel C_m,m}$  are the components of wave vector  $\mathbf{k}_m$  normal and parallel to the direction of optic axis  $C_m$ , which is also the direction of electric field in the  $m^{\text{th}}$  layer. And  $n_{e,m}$  and  $n_{o,m}$  are the extraordinary and ordinary refractive indices of the  $m^{\text{th}}$  layer, respectively. After obtaining  $k_{\perp C_m,m}$  and  $k_{\parallel C_m,m}$ , the normal-to- $C_m$  component of wave vector in the  $(m + 1)^{\text{th}}$  layer  $k_{\parallel C_m,m+1}$  can be determined according to the boundary matching of tangential wave vectors:

$$k_{\parallel C_m,m+1} = k_{\parallel C_m,m}. \quad (8)$$

To calculate the wave vector in the  $(m + 1)^{\text{th}}$  layer, we need to do a coordinate transformation as below:

$$\begin{cases} k_{\perp C_{m+1},m+1} = k_{\perp C_m,m+1} \sin \beta + k_{\parallel C_m,m+1} \cos \beta \\ k_{\parallel C_{m+1},m+1} = k_{\perp C_m,m+1} \sin \beta - k_{\parallel C_m,m+1} \sin \beta \end{cases}. \quad (9)$$

Here,  $\beta_m = \alpha_m - \alpha_{m+1}$  is the angle between optic axes in the  $m^{\text{th}}$  and the  $(m + 1)^{\text{th}}$  layers. Then we plug Eq. (9) into the following equation for wave vector  $\mathbf{k}_{m+1}$ :

$$\frac{k_{\perp C_{m+1},m+1}^2}{n_{e,m+1}^2} + \frac{k_{\parallel C_{m+1},m+1}^2}{n_{o,m+1}^2} = k_0^2. \quad (10)$$

By solving Eqs. (9) and (10), we can obtain  $k_{\perp C_m, m+1}$ . The phase change of TM polarization in the  $m^{\text{th}}$  layer is:

$$\phi_{TM, m} = \frac{2\pi}{\lambda} n_{\text{eff}, m} t_{TM, m}, \quad (11)$$

where  $n_{\text{eff}, m}$  is the effective refractive index and  $t_{TM, m}$  is the optical path of TM polarization in the  $m^{\text{th}}$  layer, respectively.

The direction of TM polarization in the  $(m+1)^{\text{th}}$  with respect to the vertical direction is:

$$\theta_{m+1} = 90^\circ - \tan^{-1} \left( \frac{k_{\perp C_m, m+1}}{k_{// C_m, m+1}} \right) - \alpha_m. \quad (12)$$

To iterate the process, we plug Eq. (12) into Eq. (3) and calculate Eqs. (7)-(12) again for computing the refraction effect of TM polarization for the next two layers until the rays arrive at the top substrate.

After computing the phase change for TE and TM in each layer, we use Eq. (13) to calculate the phase retardation and Eq. (14) for the transmittance of light:

$$\Gamma = \sum_m \phi_{TM, m} - \sum_m \phi_{TE, m}, \quad (13)$$

$$T = \sin^2(\Gamma / 2). \quad (14)$$

### 3. Results

#### 3.1 Simulation vs. experiments

To compare the refraction model with experimental results, we prepared an IPS-BPLC sample using JC-BP06. The blue phase precursor consists of 88.17 wt. % liquid crystal host JC-BP06N (JNC) with 2.92 wt.% of chiral dopant R5011 (HCCH), 5.24 wt.% di-functional reactive monomer RM257 (Merck), 3.46 wt.% TMPTA (1,1,1-Trimethylolpropane Triacrylate, Sigma Aldrich) and 0.21 wt.% photoinitiator. Then we filled the precursor into an IPS-5/5 cell in its isotropic phase. The IPS cell is comprised of interdigitated pixel electrodes on the bottom substrate, but without polyimide alignment layer. The cell gap is  $7.5 \mu\text{m}$ . Next, the cell was placed on a Linkam heating/freezing stage controlled by a temperature programmer (Linkam TMS94). The cell was cooled to the temperature near the transition temperature from chiral nematic phase to blue phase and then cured at BP-I phase with a UV light ( $\lambda \sim 365 \text{ nm}$  and intensity  $\sim 2 \text{ mW/cm}^2$ ) for 30 min.

After UV curing, nanostructured BPLC composites were self-assembled. The measured Bragg reflection wavelength is  $\lambda_B \sim 380 \text{ nm}$ . Afterwards, the IPS cell was sandwiched between two crossed polarizers for measurement. It's worth mentioning that in [30], the VT curves were measured under crossed ( $T_{\perp}$ ) and parallel ( $T_{//}$ ) polarizers, respectively; and then calculated the normalized transmittance as  $T_{\perp} / (T_{\perp} + T_{//})$ . However, this normalization method only measures the VT curve of the 0th order of diffraction and usually shows higher operation voltage and transmittance than real. Therefore, in our experimental setup we focused the transmitted light with a lens so that different diffraction orders can be collected by the detector. We measured the VT curve of the sample with this lens and normalized the transmittance to that of two open polarizers.

Figure 4 compares the simulated VT curves using Ge's and refraction models with the experimental data (IPS-5/5 at  $\lambda = 633 \text{ nm}$ ). The red solid line in Fig. 4 represents the measured VT curve. The black solid line shows the simulated VT curve using Ge's model. The general trend is similar, but the peak transmittance is lower than that of measured value. However, when we take the refraction effect into account the simulated VT curve (blue line)

overlaps with the experimental data well. So our refraction model describes the VT characteristics of IPS-BPLC quite accurately.

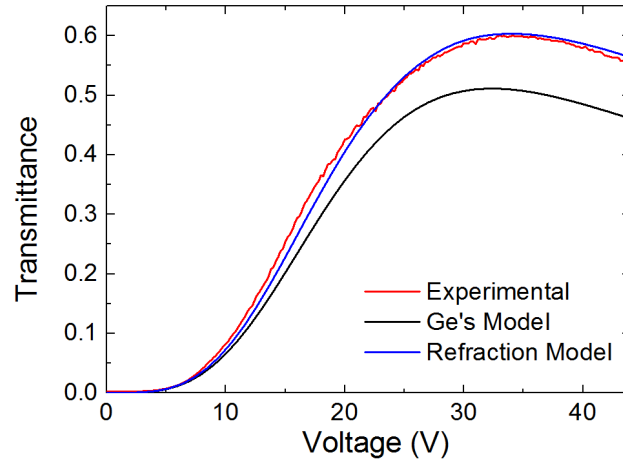


Fig. 4. Comparison between experimental VT curve and simulated results using Ge's model [18] and the refraction model. BPLC cell: JC-BP06 in IPS-5/5 at 25°C and  $\lambda = 633$  nm. The parameters used in the refraction model are  $\Delta n_s = 0.09$  and  $E_s = 2.2$  V/ $\mu\text{m}$ .

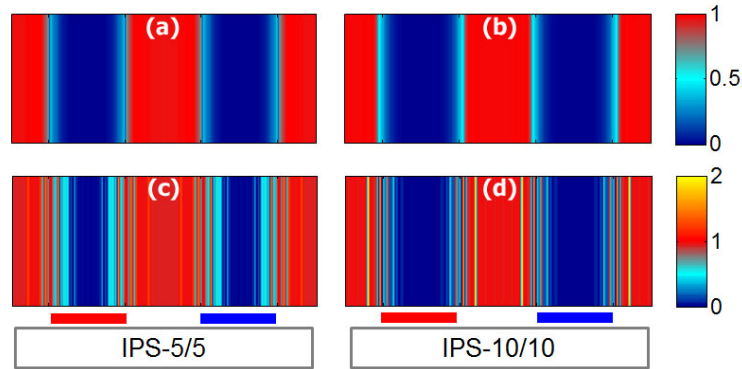


Fig. 5. Simulated transmittance profiles of JC-BP01 in (a, c) IPS-5/5 and (b, d) IPS-10/10 at  $\lambda = 633$  nm and 25°C. Cell gap  $d = 7.5$   $\mu\text{m}$ . (a, b): Ge's model, and (c, d): refraction model.

It was reported in [30] that the transmittance profiles of IPS-5/5 and 10/10 at their voltage-on state using JC-BP01 are different under the polarizing optical microscope: the IPS-5/5 sample shows an increased aperture ratio of  $\sim 75\%$  while IPS-10/10 keeps at the expected  $\sim 50\%$ . From Ge's model, both IPS-5/5 and IPS-10/10 cells exhibit  $\sim 50\%$  aperture ratios, as shown in Figs. 5(a) and 5(b), because only the induced  $\Delta n$  from electrode gaps contribute to the overall transmittance. Our refraction model can also explain well the difference in aperture ratios. Figures 5(c) and 5(d) depict the position dependent transmittance profiles of these two cells at their voltage-on states, respectively. Due to refraction, some rays penetrate into the electrode region, especially at the edges of the electrodes. This is why in [30] the electrode edges look brighter than electrode gaps. The lower aperture ratio of IPS-10/10 can be explained as follows: the light at electrode edges (where the electric fields are mostly inclined) cannot be refracted towards the center of the electrode as much as the IPS-5/5 cell because of its larger electrode dimension and same cell gap ( $d = 7.5$   $\mu\text{m}$ ). More detailed explanation of this phenomenon including the discussion of electrode dimension and cell gap effects will be addressed later.

In brief, our refraction model explains well the increased aperture ratio experimentally observed in IPS-5/5 versus IPS-10/10 BPLC cells. Therefore, our refraction model can be used to accurately predict the electro-optic properties of IPS-BPLC. From here on, we will use this model to optimize the BPLC device designs.

### 3.2 Electrode dimension effect

The electrode dimension plays an important role in the electro-optics of IPS-BPLC. Figure 6(a) shows the simulated VT curves of JC-BP01 IPS-BPLC with different electrode dimensions ( $l/w = 1$ ) using our refraction model. The fitting parameters for JC-BP01 at  $\lambda = 550$  nm are  $\Delta n_s = 0.154$  and  $E_s = 4.05$  V/ $\mu\text{m}$ . Their on-state voltages and peak transmittances are listed in Table 1. For comparison, we also included the peak transmittance calculated by Ge's model and the gained transmittance resulted from the described refraction effect.

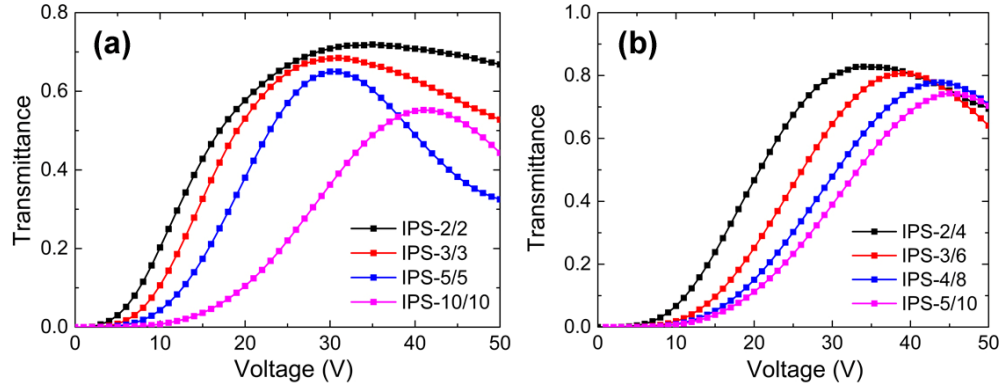


Fig. 6. Simulated VT curves of IPS cells with (a)  $l/w = 1$  and (b)  $l/w = 2$  using JC-BP01 at  $25^\circ\text{C}$  and  $\lambda = 550$  nm.

**Table 1. Comparison between refraction and Ge's [18] models for IPS-BPLC cells with  $l/w = 1$ . BPLC: JC-BP01 at  $25^\circ\text{C}$  and  $\lambda = 550$  nm**

Dimension	Refraction Model		Ge's Model $T_{\text{max}}$	Gain
	$V_{\text{on}}$ (V <sub>rms</sub> )	$T_{\text{max}}$		
IPS-2/2	34.2	0.714	0.504	41.7%
IPS-3/3	31.8	0.685	0.502	36.5%
IPS-5/5	32.4	0.650	0.507	28.2%
IPS-10/10	41.2	0.549	0.506	8.5%

As shown in Fig. 6(a), the on-state voltage ( $V_{\text{on}}$ ) decreases as electrode dimension decreases from IPS-10/10 to -5/5 and then -3/3. However, for IPS-2/2 this trend is reversed. To explain this, we need to consider two determining factors for  $V_{\text{on}}$ : penetration depth of electric field and induced birefringence  $\Delta n$ . A smaller electrode dimension requires a lower voltage to achieve comparable induced birefringence, that's why IPS-3/3 shows a lower  $V_{\text{on}}$  than IPS-5/5 and -10/10 as mentioned above. On the other hand, a smaller electrode dimension also leads to a shallower penetration depth, which in turn demands a larger induced birefringence in order to accumulate sufficient phase retardation for achieving high transmittance. These two factors compete with each other and result in a higher  $V_{\text{on}}$  for IPS-2/2 because the deficiency of shallow penetration depth outweighs the merit of strong electric field. However, for IPS-3/3 and 5/5, although their electric field intensities are weaker than that of IPS-2/2, their deeper penetration helps to lower  $V_{\text{on}}$ . Another clear trend shown in Fig. 6(a) is that the peak transmittance decreases as the electrode dimension increases. IPS-BPLCs with different electrode dimensions have different on-state voltages and electric field intensities. According to the extended Kerr model, stronger electric field would result in a higher induced  $\Delta n$ . As a result, the difference in refractive indices between neighboring layers

would be larger as explained above and the light would bend more by the refraction effect. Especially on the top of electrodes, the larger angle with respect to the optical axis and higher  $\Delta n$  would result in a higher transmittance and reduced dead zones. This is why IPS-5/5 exhibits a larger aperture ratio than IPS-10/10.

Next, we use our refraction model to simulate the VT curves of IPS-BPLC (JC-BP01) with  $l/w = 2$ , as depicted in Fig. 6(b). Table 2 lists the on-state voltage and peak transmittance with and without the refraction effect. The  $l/w = 2$  cells show following similar trend to  $l/w = 1$ : as the electrode dimension increases the peak transmittance decreases. Although a larger  $l$  leads to a deeper penetration depth, the electric field is weaker so that the induced birefringence is smaller. Moreover, a larger electrode width ( $w$ ) causes more dead-zone area, which in turn lowers the transmittance. From Table 1 and Table 2, we find that the cells with  $l/w = 2$  have less refraction effect than the  $l/w = 1$  cells. This originates from that the IPS cells with a larger  $l/w$  ratio generates a flatter electric field profile so that the incident light is less affected by the refraction effect. As a result, in comparison with Ge's model, the increase in peak transmittance due to refraction effect is smaller. We also simulated the VT curves for IPS-BPLC with  $l/w = 3$  and 4 ratios. The results are also included in Table 2, and they show the same trend as expected.

**Table 2. Comparison between refraction model and Ge's model [18] for IPS-BPLC with  $l/w = 2, 3$  and 4 structures. BPLC: JC-BP01 at 25°C and  $\lambda = 550$  nm**

Dimension	Refraction Model		Ge's Model $T_{\max}$	Gain
	$V_{\text{on}}$	$T_{\max}$		
IPS-2/4	34.2V	0.828	0.641	29.1%
IPS-3/6	38.4V	0.807	0.637	26.7%
IPS-4/8	42.8V	0.778	0.641	21.3%
IPS-5/10	44.6V	0.743	0.643	15.6%
IPS-2/6	41.8V	0.846	0.733	15.5%
IPS-3/9	44.2V	0.836	0.737	13.4%
IPS-2/8	48.2V	0.866	0.785	10.3%
IPS-3/12	49.6V	0.832	0.783	6.3%

### 3.3 Cell gap effect

In a nematic IPS cell, both transmittance and response time are affected by the cell gap. However, the transmittance of IPS-BPLC is insensitive to the cell gap as long as the cell gap exceeds the penetration depth of electric field [17]. This feature is particularly desirable for fabricating large LCD panels, in which uniform cell gap control is a big concern. Here we revisit this important feature by including the refraction effect.

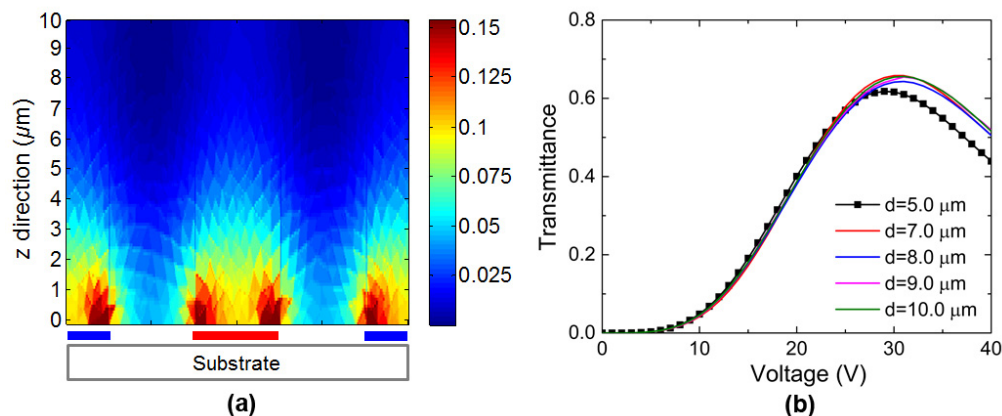


Fig. 7. (a) Induced  $\Delta n$  profile of a 10- $\mu\text{m}$ -thick IPS-5/5 cell at 31V and (b) simulated VT curves of IPS-5/5 with different cell gaps using JC-BP01 (25°C and  $\lambda = 550$  nm).

Figure 7(a) depicts the induced birefringence distribution of a 10- $\mu\text{m}$ -thick IPS-5/5 cell and Fig. 7(b) shows the VT curves of the IPS-5/5 cell with different cell gaps simulated by our refraction model. The material employed here is JC-BP01. From Fig. 7(a), the induced birefringence is the largest near the electrode surface and it gradually decreases as the distance increases. For JC-BP01, as the depth increases to 5.5  $\mu\text{m}$  the induced birefringence decreases to 0.05. Hence, for IPS-BPLC the VT curve is insensitive to cell gap as long as the cell gap is larger than the field's penetration depth, which is governed by the electrode dimension through Poisson equation. This is verified in Fig. 7(b). Therefore, similar to Ge's model our refraction model also shows that the VT curve is indeed insensitive to the cell gap variation, as long as the cell gap is above the field's penetration depth.

Shown in Figs. 8(a)-(d) are the spatial transmittance profiles of IPS-5/5 with cell gap  $d = 5, 7, 8,$  and  $10 \mu\text{m}$ , respectively. As the cell gap increases, the light would be bent more toward the center of the electrode by the refraction effect due to its longer optical path. This explains why the IPS-5/5 with  $d = 10 \mu\text{m}$  (Fig. 8(d)) shows a slightly larger aperture ratio than the corresponding 7- $\mu\text{m}$  cell (Fig. 8(b)). Nevertheless, the electric fields beyond the penetration regions are very weak and the BPLC in that region can be regarded as isotropic, so the light wouldn't accumulate additional phase retardation and transmittance wouldn't change although they have longer optical path. As a result, the VT curves are not critically dependent on the cell gap as long as the cell gap is larger than the field's penetration depth. Moreover, the cell gap effect can be used to explain the above mentioned lower aperture ratio of IPS-10/10 because its larger electrode dimension.

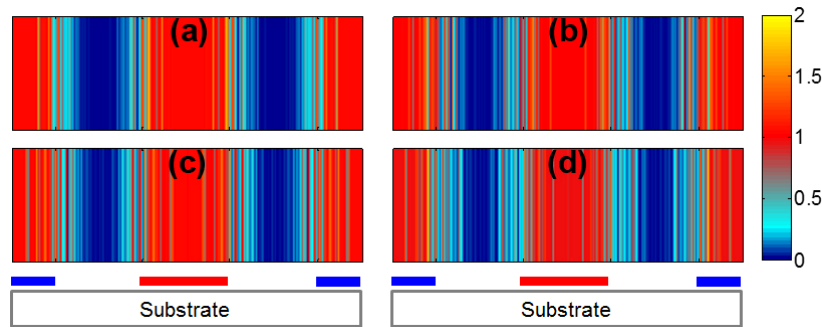


Fig. 8. Transmittance profile of IPS-5/5 with different cell gaps: (a) 5  $\mu\text{m}$ , (b) 7  $\mu\text{m}$ , (c) 8  $\mu\text{m}$  and (d) 10  $\mu\text{m}$ . BPLC: JC-BP01 at 25°C and  $\lambda = 550 \text{ nm}$ .

### 3.4 Saturated birefringence and saturation field effects

A larger saturated birefringence  $\Delta n_s$  not only helps boost the Kerr constant [2] but also makes direct impact on the electro-optics due to the refraction effect. Based on JC-BP01, Fig. 9(a) shows the simulated VT curves of IPS-2/4 with different  $\Delta n_s$  while keeping  $E_s$  unchanged ( $E_s = 4.05 \text{ V}/\mu\text{m}$ ). The red dashed lines represent JC-BP01. As  $\Delta n_s$  increases, the peak transmittance increases while on-state voltage decreases. For a BPLC with higher  $\Delta n_s$ , according to Eq. (2), the refractive index difference between neighboring layers would increase and the light would bend more. Thus, the light would propagate at a larger angle with respect to the optical axis. Moreover, a higher  $\Delta n_s$  helps enhance phase retardation. These two factors combine together to result in a higher transmittance and reduced dead zones.

Figure 9(b) shows how  $E_s$  affects the VT curves of IPS-2/4 based on JC-BP01. It's clearly shown that as  $E_s$  increases the on-state voltage also increases while peak transmittance remains unchanged. This indicates that  $E_s$  only determines the voltage where the BPLC reaches its  $\Delta n_s$ , but the maximum induced  $\Delta n$  still remains unchanged at the on-state voltage.

Therefore, in IPS-BPLC structures a larger  $\Delta n_s$  helps reduce the operation voltage and enhance the transmittance, not only from increasing the Kerr constant on material side but

also from stronger refraction effect in the cell. A smaller  $E_s$  is effective in lowering operation voltage but doesn't affect the peak transmittance. In order to achieve low voltage while keeping high transmittance, we should boost  $\Delta n_s$  while keeping  $E_s$  low.

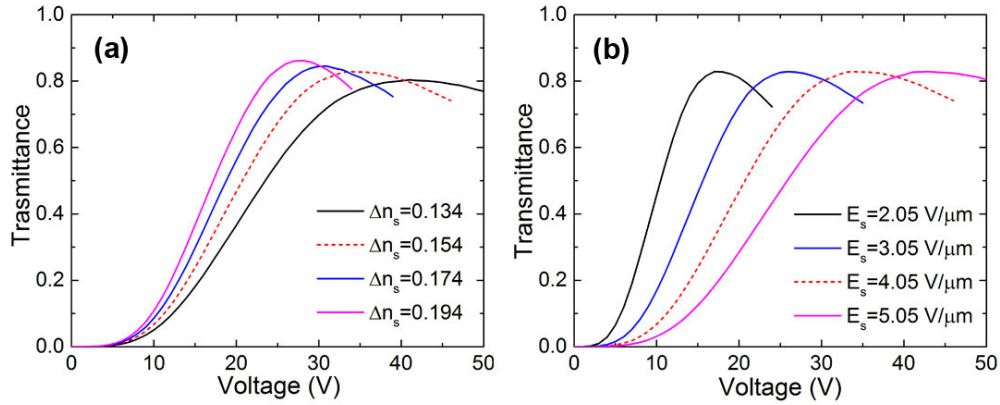


Fig. 9. Simulated VT curves of IPS-2/4 using BPLCs with (a) different  $\Delta n_s$  but same  $E_s = 4.05$  V/ $\mu\text{m}$ , and (b) different  $E_s$  but same  $\Delta n_s = 0.154$  at  $25^\circ\text{C}$  and  $\lambda = 550$  nm. Red dashed lines: JC-BP01.

### 3.5 Protruded electrodes

Based on the discussion above, we can enhance the transmittance by increasing the  $l/w$  ratio of an IPS structure. The reasons are twofold: 1) a larger  $l/w$  ratio leads to smaller dead zone area, and 2) it increases the field's penetration depth. However, the major tradeoff is increased voltage because of the wider electrode gap. An effective way to overcome this problem is to employ protrusion electrodes [21, 32], which enable the horizontal electric fields to penetrate deeply into the bulk LC layer. The detailed performance depends on the protrusion height and the  $l/w$  ratio.

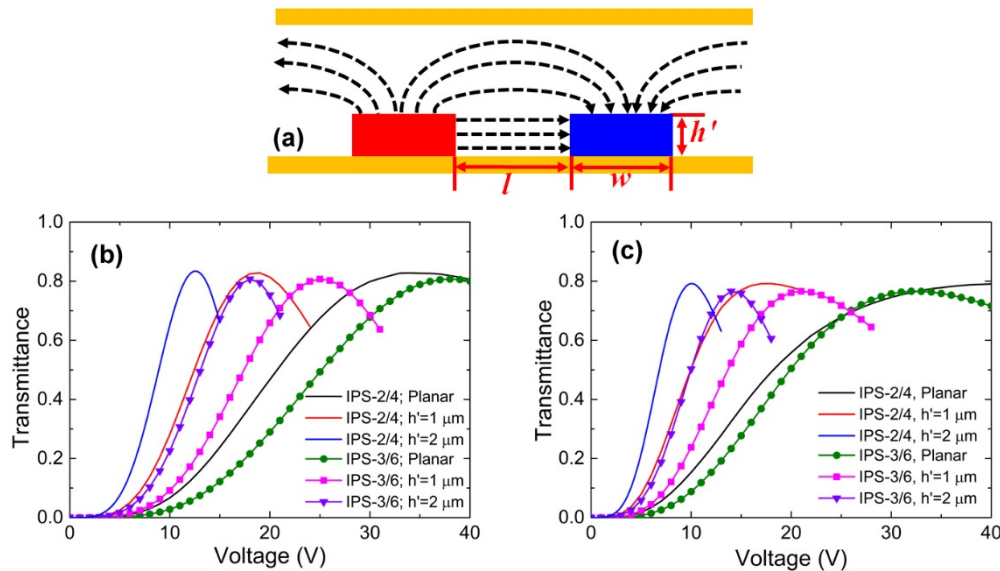


Fig. 10. (a) Cell structure and parameter definitions of protrusion IPS-BPLC, and simulated VT curves of the protrusion IPS-BPLC with different electrode dimensions employing (b) JC-BP01 and (c) JC-BP06 ( $25^\circ\text{C}$  and  $\lambda = 550$  nm).

To investigate the influence of refraction effect on the transmittance of protruded IPS cell, we used rectangular protruded electrodes in our simulations, as depicted in Fig. 10(a). Shown in Figs. 10(b) and 10(c) are the simulated VT curves of planar and protruded IPS cells with protrusion height  $h' = 1 \mu\text{m}$  and  $2 \mu\text{m}$  for IPS-2/4 and IPS-3/6 employing two different BPLC materials: JC-BP01 ( $\Delta n_s = 0.154$ ,  $E_s = 4.05 \text{ V}/\mu\text{m}$ ) and JC-BP06 ( $\Delta n_s = 0.09$ ,  $E_s = 2.2 \text{ V}/\mu\text{m}$ ). Compared to a planar IPS, the protruded IPS shows about the same transmittance because the protrusion electrodes mainly generate electric fields in the electrode gaps and don't change the field distribution above the electrodes. But due to the dimension effect described above, IPS-3/6 exhibits a slightly lower transmittance than IPS-2/4 with the same protrusion height. From the comparison of these curves, we find that by enhancing the protrusion height the operation voltage can be reduced dramatically. However, high-protrusion electrodes are more difficult to make with current fabrication technique. On the other hand, JC-BP06 shows a higher voltage than JC-BP01 for planar IPS-2/4 structure (40V vs. 34V). This is because JC-BP06 has a relatively small induced birefringence ( $\Delta n_s = 0.09$ ) and IPS-2/4 has a relatively shallow penetration depth. Thus, it requires a higher operation voltage to reach the peak transmittance. However, when we utilize protrusion electrodes, the relatively small  $\Delta n_s$  of JC-BP06 can be compensated with the increased penetration depth. Therefore, with the same device structure JC-BP06 exhibits a lower operation voltage than JC-BP01 because JC-BP06 has a larger Kerr constant. As Fig. 10(c) shows, for IPS-2/4 with  $h' = 2 \mu\text{m}$  its operation voltage is reduced to 10V while keeping 80% transmittance. This is an important milestone to enable BPLC to be addressed by a-Si TFT technology. To boost transmittance further, we can increase the birefringence of the BPLC material. For example as Fig. 10(b) shows, JC-BP01 has a higher induced birefringence so that its peak transmittance can reach 83%.

### 3.6 Etched electrodes

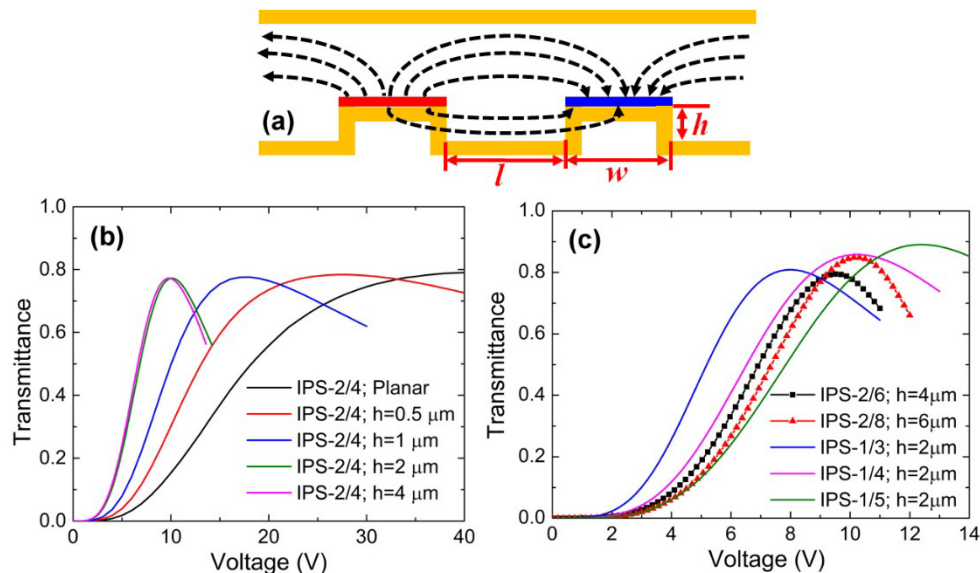


Fig. 11. (a) Cell structure and parameter definitions of etched-IPS, and simulated VT curves of etched-IPS cells with different electrode dimensions: (b)  $l/w = 2$  and (c)  $l/w = 3, 4$  and  $5$  using JC-BP06 ( $25^\circ\text{C}$  and  $\lambda = 550 \text{ nm}$ ).

In contrast to protruded electrodes, etching is another option to lower the operation voltage [28, 33]. The cell structure of an etched-IPS is depicted in Fig. 11(a). In an etched-IPS structure, say IPS-2/4, the etching takes place along the  $4\text{-}\mu\text{m}$  electrode gaps. As a result, the fringe fields are above and under the  $2\text{-}\mu\text{m}$  ITO electrodes. These doubled penetrating fringe

fields help to reduce the operation voltage. Similar to protruded IPS, etched-IPS using JC-BP06 also shows lower operation voltage than that using JC-BP01 since the bottom fringe fields provide an extra phase retardation to compensate for the relatively small  $\Delta n_s$  of JC-BP06. Therefore, in our simulation we use JC-BP06 as an example to demonstrate the effectiveness of this etched-electrode approach.

Figure 11(b) compares the simulated VT curves of IPS-2/4 structure with etching depth  $h$  increasing from 0, 0.5, 1, 2 to 4  $\mu\text{m}$ . As the etching depth increases, the operation voltage decreases rapidly and then gradually saturates. With  $h \sim 2 \mu\text{m}$ , the operation voltage is reduced to  $\sim 10 V_{\text{rms}}$ . This saturation phenomenon has been reported in [28], which originates from the finite penetration depth of the electric field. Hence, when the etching depth is larger than the penetration depth, the operation voltage does not decrease anymore. This feature makes the etched-electrode IPS easy to fabricate since we don't need to control the etching depth very precisely as long as it's larger than the penetration depth. Similar to the protruded IPS, the etched electrodes have minor influence on the transmittance since the electric field distribution on the top of the electrode is not changed.

To improve transmittance, we can increase the  $l/w$  ratio, such as IPS-2/6 or -2/8, while still using the etched electrodes. Similar to the etched IPS-2/4, both etched IPS-2/6 and -2/8 show the saturation effect, but at a deeper etching depth (4  $\mu\text{m}$  for IPS-2/6 and 6  $\mu\text{m}$  for IPS-2/8), due to their larger penetration depths. Figure 11(c) includes the simulated VT curves of etched IPS-2/6 and IPS-2/8 cells with 4- $\mu\text{m}$  and 6- $\mu\text{m}$  etching depths, respectively. Compared to IPS-2/4, although their transmittance can exceed 80% due to their larger  $l/w$  ratios, a tradeoff is increased voltage. As nanotechnology advances, smaller electrode dimension could be fabricated. If we can reduce the electrode width to 1  $\mu\text{m}$ , then the operation voltage as low as 8V while keeping transmittance  $>80\%$  can be achieved, as Fig. 11(c) shows.

In addition to optimizing device structures, continuous development on large Kerr constant materials [25, 26] would help to further reduce the operation voltage. From Gerber's model [34], Kerr constant is mainly determined by the  $\Delta n \cdot \Delta \epsilon$  of the LC host, assuming the pitch length and average elastic constant remain the same. The two BPLC materials we used in simulations are JC-BP01 ( $\Delta n_s = 0.154$ ,  $E_s = 4.05 \text{ V}/\mu\text{m}$ ) and JC-BP06 ( $\Delta n_s = 0.09$ ,  $E_s = 2.2 \text{ V}/\mu\text{m}$ ). JC-BP01 has a reasonably large  $\Delta n_s$ , but its  $E_s$  is too high, i.e.,  $\Delta \epsilon$  is not large enough. On the contrary, although JC-BP06 has a large  $\Delta \epsilon$ , its  $\Delta n_s$  is too low. For future material improvement, we should not only emphasize on increasing the Kerr constant, but also need to pay attention to the individual  $\Delta n$  and  $\Delta \epsilon$  values.

### 3.7 IPS-BPLC with a single gamma curve

In an IPS-BPLC cell, the phase retardation depends on the wavelength and induced birefringence. The latter in turn depends on the Kerr constant, which decreases as the wavelength increases [35]. Therefore, the VT curves of an IPS-BPLC depend on the wavelength, as shown in Fig. 12(a), and three gamma curves are required to drive the red ( $R = 650 \text{ nm}$ ), green ( $G = 550 \text{ nm}$ ) and blue ( $B = 450 \text{ nm}$ ) sub-pixels, which increases the complexity of driving electronics.

To solve this problem, we propose following method to achieve single gamma curve for IPS-BPLC. Based on the discussion above, we know that the on-state voltage of an IPS-BPLC can be adjusted by changing the  $l/w$  ratios. Therefore, in order to achieve overlapped gamma curves for RGB colors, we can simply vary the electrode gap ( $l$ ) for RGB sub-pixels while keeping the same electrode width ( $w$ ) and etching depth ( $h$ ). Similar approach of adjusting the electrode gap has been reported in [36] to balance the optical phase retardation between transmissive and reflective regions for transreflective displays. Here, let us continue to use IPS-2/4 with  $h = 2.5 \mu\text{m}$  and  $d = 7.5 \mu\text{m}$  for the green wavelength to illustrate the design principles. From Fig. 12(a), we need to lower the on-state voltage for the red color. Thus, we choose a smaller electrode gap, say  $l = 3.6 \mu\text{m}$ , while still keeping  $h = 2.5 \mu\text{m}$  and  $d = 7.5 \mu\text{m}$ . On the other hand, we increase  $l$  to  $5.2 \mu\text{m}$  for the blue wavelength. Figure 12(b) shows the

normalized VT curves for the unequally-spaced IPS cell. Indeed, the RGB gamma curves overlap fairly well.

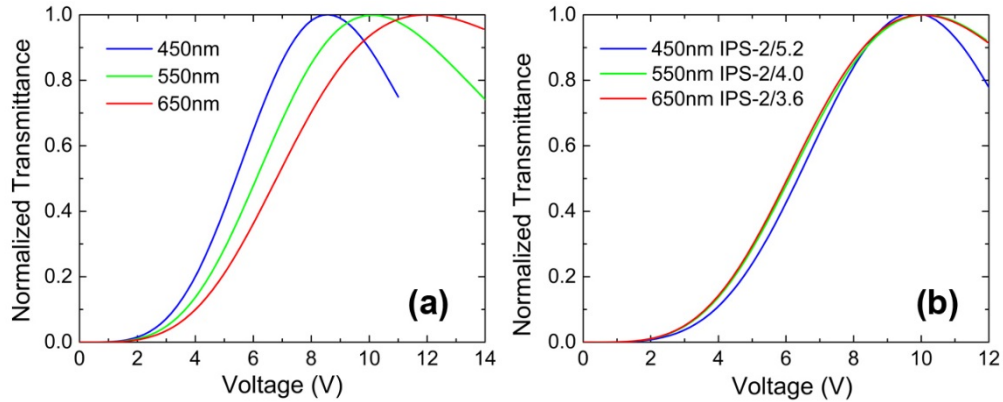


Fig. 12. (a) Simulated VT curves for RGB wavelengths. BPLC cell: etched IPS-2/4 with  $h = 2.5 \mu\text{m}$  and JC-BP06, and (b) Simulated VT curves for IPS-2/3.6 (R), -2/4 (G), -2/5.2 (B) with  $h = 2.5 \mu\text{m}$  and  $d = 7.5 \mu\text{m}$ .

#### 4. Conclusion

We propose a numerical model to account for the refraction effect in an IPS-BPLC cell. Our model agrees with experiment quite well. Based on this model, different effects, such as electrode dimension, cell gap, saturated birefringence and saturation electric field, on the electro-optics of IPS-BPLC cells are investigated in a more insightful way. In addition, we use the refraction model to study the electro-optics of different IPS structures, including planar, protruded electrodes and etched electrodes. An IPS-BPLC with operation voltage  $<10\text{V}$  and transmittance  $>80\%$  can be achieved. Moreover, IPS-BPLC with single gamma curve can be achieved by optimizing the  $l/w$  ratios for RGB sub-pixels.

#### Acknowledgments

The authors are indebted to Industrial Technology Research Institute (ITRI), Taiwan, for the financial support.